Received February 2001
Accepted February 2001

Accurate and efficient solutions of unsteady viscous flows

P. De Palma
Dipartimento di Ingegneria Meccanica, Università degli Studi di Roma "Tor Vergata", Rome, Italy
G. Pascazio and M. Napolitano
Dipartimento di Ingegneria, Meccanica e Gestionale, Politecnico di Bari, Bari, Italy

Keywords *Flow, Unsteady computation, Viscous flows*

Abstract *This paper describes two accurate and efficient numerical methods for computing unsteady viscous flows. The first one solves the incompressible Navier-Stokes equations in their vorticity-velocity formulation, using a staggered-grid finite-volume spatial discretization to provide second-order accuracy on arbitrary grids, and combines effectively an alternating direction implicit scheme for the vorticity transport equation and a multigrid line-Gauss-Seidel relaxation for the velocity equations. The second method solves the compressible Reynolds-averaged Navier-Stokes equations in strong conservation form, with a* $k-\omega$ *turbulence closure model. The equations are discretized in time using an implicit three-time-level scheme, combined with a dual time stepping approach, so that the residual at every physical time step is annihilated using an efficient multigrid Runge-Kutta iteration with variable time stepping and implicit residual smoothing. The space discretization uses a Roe's flux difference splitting for the convective terms and standard central differences for the diffusive ones. A turbulent unsteady cascade flow is used to demonstrate the accuracy and efficiency of the method. The authors are currently working towards extending the two approaches described in this paper to three space dimensions.*

1. Introduction

This paper describes two methods recently developed by the authors to compute unsteady viscous flows.

The first approach employs the vorticity-velocity formulation of the incompressible Navier-Stokes equations, originally proposed by Fasel (1976), for which the authors developed a very accurate method for solving two-dimensional steady flows in general boundary-fitted coordinates (Pascazio and Napolitano, 1996). The governing equations are written as a system of a scalar vorticity transport equation and a second-order equation for the velocity vector – obtained by combining the vorticity definition and the incompressibility condition – and discretized in space by a staggered-grid second-order-accurate finite-volume method. The vorticity transport equation is discretized in time by means of an implicit three-level scheme solved by means of an alternating direction implicit method, and the two second-order elliptic velocity equations are solved by means of a very efficient multigrid line-Gauss-Seidel relaxation

International Journal of Numerical Methods for Heat & Fluid Flow, Vol. 11 No. 4, 2001, pp. 286-307.

This work has been supported by MURST.

scheme. An inner iteration is performed for computing the wall vorticity in terms of the updated velocity field, so as to achieve second-order accuracy in time and to satisfy the discrete counterparts of the vorticity definition and of the continuity equation within any desired accuracy level. Results are presented which demonstrate the accuracy and efficiency of the method.

The second approach solves the compressible Navier-Stokes equations written in strong conservation form plus the $k-\omega$ turbulence-model equations by a strongly coupled approach, namely, as a unique set. The convective and diffusive terms in the equations are discretized by a second-order-accurate upwind Roe's scheme (Roe, 1981) and central differences, respectively. Second-order accuracy in time is obtained using a three-level backward discretization of the physical time derivative and a dual time stepping technique (Arnone *et al.*, 1995): a four-stage Runge-Kutta time integration scheme, with local time stepping, implicit residual smoothing, and multigrid, is employed to achieve fast convergence of the false transient problem to be solved at each physical time level. The unsteady turbulent flow past a turbine cascade is used as a suitable problem to demonstrate the accuracy and efficiency of the method.

2. Incompressible flows

2.1 Governing equations

The two-dimensional incompressible vorticity-velocity Navier-Stokes equations are written in conservative form as:

$$\frac{\partial \omega}{\partial t} + \nabla \cdot (\boldsymbol{u}\omega) - \frac{1}{Re}\nabla^2 \omega = 0, \tag{1}$$

$$\nabla \cdot \boldsymbol{u} = 0, \tag{2}$$

$$\nabla \times \boldsymbol{u} = \omega \boldsymbol{k}, \tag{3}$$

where $\boldsymbol{u}$ is the velocity vector, ω is the only component of ω, $\boldsymbol{k}$ is the unit vector in the direction normal to the plane of the flow, t is the time, and Re is the Reynolds number. The problem stated in equations (1)-(3) is written in the so-called *div-curl* formulation and can be solved numerically as it is (see, for example, Osswald *et al.* (1987); Gatski *et al.* (1989)). However, from a computational standpoint, it is convenient to obtain a second-order elliptic PDE for the velocity vector in place of the two first-order scalar equations (2) and (3), so as to use standard relaxation methods, while satisfying equations (2) and (3) exactly in the discrete. Following Pascazio and Napolitano (1996), one subtracts the gradient of equation (2) from the *curl* of equation (3), to obtain:

$$\nabla \times \nabla \times \boldsymbol{u} - \nabla(\nabla \cdot \boldsymbol{u}) = \nabla \times \omega \boldsymbol{k}. \tag{4}$$

By virtue of Gauss's theorem, equations (1) and (4) are written in integral form as:

$$\frac{\partial}{\partial t}\int_{\mathcal{V}} \omega d\mathcal{V} + \oint_S \left(\boldsymbol{u}\omega - \frac{1}{Re}\nabla\omega\right)\cdot d\boldsymbol{S} = 0, \tag{5}$$

$$\oint_S (\nabla \times \boldsymbol{u}) \times d\boldsymbol{S} + \oint_S (\nabla \cdot \boldsymbol{u}) d\boldsymbol{S} - \oint_S \omega \boldsymbol{k} \times d\boldsymbol{S} = 0, \tag{6}$$

where $\mathcal{V}$ and S are the control volume and the surface enclosing it, respectively (an area and a line in the present two-dimensional context).

2.2 Numerical method

Equations (5) and (6) are discretized in space as:

$$\mathcal{V}\frac{\partial \omega}{\partial t} + \sum_l \left(\boldsymbol{u}\omega - \frac{1}{Re}\nabla\omega\right)\cdot S^l = 0, \tag{7}$$

$$\sum_l (\nabla \times \boldsymbol{u} - \omega \boldsymbol{k}) \times \boldsymbol{S}^l + \sum_l (\nabla \cdot \boldsymbol{u})\boldsymbol{S}^l = 0, \tag{8}$$

where $\mathcal{V}$ and $\boldsymbol{S}^l$ indicate the cell control volume and its face area vectors, respectively, the summation being extended to all faces of $\mathcal{V}$.

In the present staggered-grid finite-volume discretization, the vorticity is defined at the nodes, whereas the discrete velocity field is approximated by means of the flow rates across the faces of the cells. With reference to the elementary cell, depicted in Figure 1, one has:

$$U = \boldsymbol{u}\cdot\boldsymbol{S}^{\xi}, \quad V = \boldsymbol{u}\cdot\boldsymbol{S}^{\eta}. \tag{9}$$

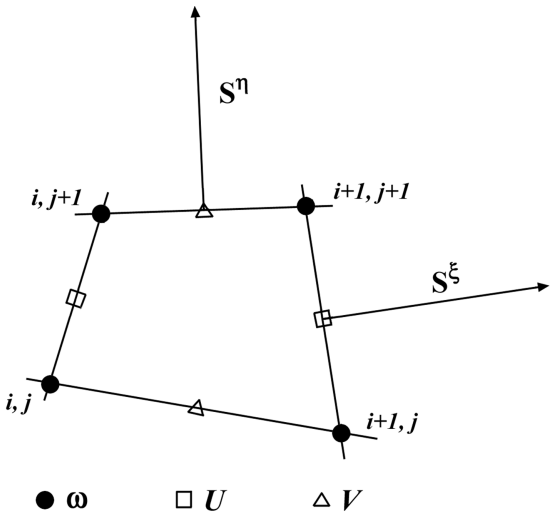

Figure 1.
Elementary finite volume

In equation (9), $\boldsymbol{S}^{\xi}$ and $\boldsymbol{S}^{\eta}$ are the vectors having magnitude equal to the face area and direction normal to it; they are provided as:

$$\begin{aligned}\boldsymbol{S}^{\xi} &= \frac{\partial \boldsymbol{r}}{\partial \eta} \times \boldsymbol{k} = y_{\eta}\boldsymbol{\imath} - x_{\eta}\boldsymbol{\jmath} = (y_{i+1,j+1} - y_{i+1,j})\boldsymbol{\imath} - (x_{i+1,j+1} - x_{i+1,j})\boldsymbol{\jmath},\\ \boldsymbol{S}^{\eta} &= -\frac{\partial \boldsymbol{r}}{\partial \xi} \times \boldsymbol{k} = -y_{\xi}\boldsymbol{\imath} + x_{\xi}\boldsymbol{\jmath} = -(y_{i+1,j+1} - y_{i,j+1})\boldsymbol{\imath}\\ &\quad + (x_{i+1,j+1} - x_{i,j+1})\boldsymbol{\jmath},\end{aligned} \tag{10}$$

where $\boldsymbol{r}$ is the position vector ($\boldsymbol{r} = (x,y)^T$), (ξ, η) are the computational-domain coordinates, and $\boldsymbol{\imath}, \boldsymbol{\jmath}$ are the unit vectors along the x and y directions, respectively. The velocity vector can thus be expressed as:

$$\boldsymbol{u} = U\boldsymbol{S}_{\xi} + V\boldsymbol{S}_{\eta}, \tag{11}$$

where $\boldsymbol{S}_{\xi}, \boldsymbol{S}_{\eta}$ are the base vectors defined as:

$$\boldsymbol{S}^{m} \cdot \boldsymbol{S}_{n} = \delta_{n}^{m}, \tag{12}$$

δ_{n}^{m} being the Kronecker delta.

The vector equation (8) is reformulated so as to give two scalar equations for the dependent variables U, V. This is accomplished by taking the dot product of equation (8) with the corresponding face area vectors, $\boldsymbol{S}^{\xi}$, $\boldsymbol{S}^{\eta}$, to give:

$$\mathcal{V}\frac{\partial U}{\partial \tau} - \boldsymbol{S}^{\xi} \cdot \left[\sum_{l}(\nabla \times \boldsymbol{u} - \omega \boldsymbol{k}) \times \boldsymbol{S}^{l} \sum_{l}(\nabla \cdot \boldsymbol{u})\boldsymbol{S}^{l}\right] = 0, \tag{13}$$

$$\mathcal{V}\frac{\partial V}{\partial \tau} - \boldsymbol{S}^{\eta} \cdot \left[\sum_{l}(\nabla \times \boldsymbol{u} - \omega \boldsymbol{k}) \times \boldsymbol{S}^{l} \sum_{l}(\nabla \cdot \boldsymbol{u})\boldsymbol{S}^{l}\right] = 0; \tag{14}$$

a relaxation-like time derivative has been added to each equation, for computational convenience.

The vorticity transport equation, equation (7), is rewritten as:

$$\mathcal{V}_{\omega}\frac{d\omega_{i,j}}{dt} = R_{i,j} = -\mathcal{C}_{i,j}(U, V, \omega) + \frac{1}{Re}\mathcal{L}_{i,j}(\omega), \tag{15}$$

where $\mathcal{V}_{\omega}$ is the vorticity control volume (ABCD in Figure 2), whereas $\mathcal{C}_{i,j}$ and $\mathcal{L}_{i,j}$ indicate the discrete convective and diffusive operators, respectively, computed as:

$$\mathcal{C}_{i,j}(U, V, \omega) = (U\omega)_{i+\frac{1}{2}} - (U\omega)_{i-\frac{1}{2}} + (V\omega)_{j+\frac{1}{2}} - (V\omega)_{j-\frac{1}{2}}, \tag{16}$$

$$\mathcal{L}_{i,j}(\omega) = (\nabla\omega \cdot \boldsymbol{S}^{\xi})_{i+\frac{1}{2}} - (\nabla\omega \cdot \boldsymbol{S}^{\xi})_{i-\frac{1}{2}}(\nabla\omega \cdot \boldsymbol{S}^{\eta})_{j+\frac{1}{2}} - (\nabla\omega \cdot \boldsymbol{S}^{\eta})_{j-\frac{1}{2}}. \tag{17}$$

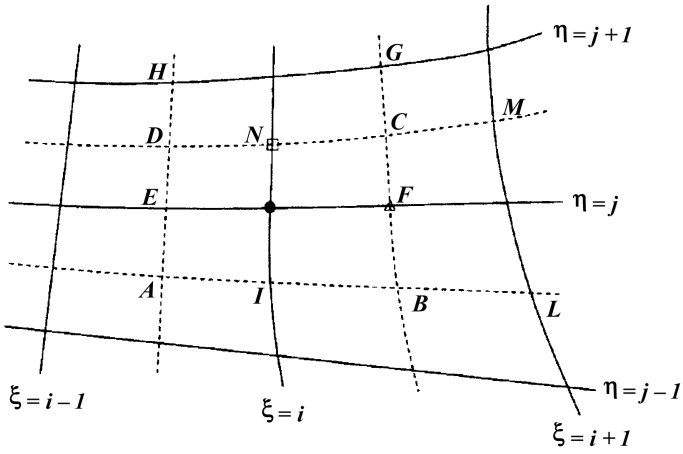

Figure 2.
Computational cells

(symbols as in Figure 1)

In the equations above, and in the following ones, standard algebraic averaging is used to compute the values of the variables ω, U, V, wherever they are not defined. Furthermore, the term $(\nabla\omega \cdot \boldsymbol{S}^{\xi})_{i+\frac{1}{2}}$ in equation (17) is a shorthand notation for $\nabla\omega_{i+\frac{1}{2},j} \cdot \boldsymbol{S}^{\xi}_{i+\frac{1}{2},j}$, where

$$\nabla\omega_{i+\frac{1}{2},j} = \frac{1}{\mathcal{V}}\left[(\omega\boldsymbol{S}^{\xi})_{i+1} - (\omega\boldsymbol{S}^{\xi})_{i} + (\omega\boldsymbol{S}^{\eta})_{j+\frac{1}{2}} - (\omega\boldsymbol{S}^{\eta})_{j-\frac{1}{2}}\right], \tag{18}$$

$$\boldsymbol{S}^{\xi}_{i+\frac{1}{2},j} = \frac{1}{4}\left[\boldsymbol{S}^{\xi}_{i,j+\frac{1}{2}} + \boldsymbol{S}^{\xi}_{i+1,j+\frac{1}{2}} + \boldsymbol{S}^{\xi}_{i,j-\frac{1}{2}} + \boldsymbol{S}^{\xi}_{i+1,j-\frac{1}{2}}\right]. \tag{19}$$

Similar expressions are used for the remaining three terms.

In the present work a three-level time integration scheme (Beam and Warming, 1980) is used:

$$\begin{aligned}\mathcal{V}_{\omega}\frac{(1+\xi)\omega^{n+1}_{i,j} - (1+2\xi)\omega^{n}_{i,j} + \xi\omega^{n-1}_{i,j}}{\Delta t} &= \left(\frac{3}{2}+\xi\right)R^{n}_{i,j} - \left(\frac{1}{2}+\xi\right)R^{n-1}_{i,j} \\ &+ \theta\left[\hat{\mathcal{C}}^{n+1}_{i,j}(\omega) - 2\,\hat{\mathcal{C}}^{n}_{i,j}(\omega) + \hat{\mathcal{C}}^{n-1}_{i,j}(\omega)\right], \\ &+ \frac{\theta}{Re}\left[\hat{\mathcal{L}}^{n+1}_{i,j}(\omega) - 2\,\hat{\mathcal{L}}^{n}_{i,j}(\omega) + \hat{\mathcal{L}}^{n-1}_{i,j}(\omega)\right],\end{aligned} \tag{20}$$

where n is the time level, Δt is the time step,

$$\left(\frac{\partial\hat{\mathcal{C}}_{i,j}}{\partial\omega}\right)^{n} = U^{n}\frac{\partial}{\partial\xi} + V^{n}\frac{\partial}{\partial\eta},$$

and ξ and θ are parameters to be selected. Equation (20) is then linearized and written in terms of the incremental unknown, $\Delta\omega^{n} = \omega^{n+1} - \omega^{n}$, as:

$$\left[(1+\xi)\Delta\omega^n + \frac{\Delta t}{\mathcal{V}_\omega}\theta\left(\frac{\partial \hat{\mathcal{C}}_{i,j}}{\partial\omega}\right)^n \Delta\omega^n - \frac{\Delta t}{\mathcal{V}_\omega}\frac{\theta}{Re}\ \hat{\mathcal{L}}_{i,j}(\Delta\omega^n)\right] = \xi\Delta\omega^{n-1}$$
$$+\frac{\Delta t}{\mathcal{V}_\omega}\theta\left(\frac{\partial \hat{\mathcal{C}}_{i,j}}{\partial\omega}\right)^n \Delta\omega^{n-1} - \frac{\Delta t}{\mathcal{V}_\omega}\frac{\theta}{Re}\ \hat{\mathcal{L}}_{i,j}(\Delta\omega^{n-1}) \tag{21}$$
$$+\frac{\Delta t}{\mathcal{V}_\omega}\left[\left(\frac{3}{2}+\xi\right)R^n_{i,j} - \left(\frac{1}{2}+\xi\right)R^{n-1}_{i,j}\right].$$

The discrete equation (21) is solved by an alternating direction implicit method using $\xi = 1/2$ and $\theta = 1$, to achieve second-order accuracy in time. The problem is closed by computing the vorticity at the boundary by the discrete form of its definition, equation (3):

$$\omega^{n+1}_{i,j}\boldsymbol{k} = \frac{\boldsymbol{k}}{\mathcal{V}_\omega}\Big[(Js^{\xi\xi}V^n - Js^{\xi\eta}U^n)_{i+\frac{1}{2}} - (Js^{\xi\xi}V^n - Js^{\xi\eta}U^n)_{i-\frac{1}{2}}$$
$$-(Js^{\eta\eta}U^n - Js^{\xi\eta}V^n)_{j+\frac{1}{2}} + (Js^{\eta\eta}U^n - Js^{\xi\eta}V^n)_{j-\frac{1}{2}}\Big], \tag{22}$$

where:

$$s^{mn} = \boldsymbol{S}^m \cdot \boldsymbol{S}^n, \quad m,n = \xi,\eta,$$
$$\frac{1}{J_{i,j}} = (x_{i+\frac{1}{2}} - x_{i-\frac{1}{2}})(y_{j+\frac{1}{2}} - y_{j-\frac{1}{2}}) - (x_{j+\frac{1}{2}} - x_{j-\frac{1}{2}})(y_{i+\frac{1}{2}} - y_{i-\frac{1}{2}}). \tag{23}$$

It is noteworthy that: i) the approximation of the diffusive term is incompletely implicit, since $\hat{\mathcal{L}}_{i,j}$ only contains the penta-diagonal entries of $\mathcal{L}_{i,j}$; ii) the time decoupling between the vorticity and velocity fields due to the use of equation (22) leads to a delay error, and thus to first-order accuracy in time. Second-order-accuracy in time can be recovered by performing an inner iteration at each time level, with the boundary vorticity computed as:

$$\left(\omega^{n+1,r+1}\boldsymbol{k}\right)_b = \left(\nabla \times \boldsymbol{u}^{n+1,r}\right)_b.$$

The inner loop is stopped when the solutions at steps $r+1$ and r coincide within a prescribed tolerance, ϵ.

Once the vorticity field has been computed at time level $n+1$, the velocity unknowns, U^{n+1} and V^{n+1}, are evaluated by solving equations (13) and (14) using a two-level implicit Euler scheme and the delta form of Beam and Warming (1978). The resulting discrete equations read:

$$\mathcal{V}_U\frac{\Delta U_{i,j+\frac{1}{2}}}{\Delta\tau} - \mathcal{L}^\xi_{i,j+\frac{1}{2}}(\Delta U, V) = \mathcal{L}^\xi_{i,j+\frac{1}{2}}(U,V) - \mathcal{D}^\xi_{i,j+\frac{1}{2}}(\omega), \tag{24}$$

$$\mathcal{V}_V \frac{\Delta V_{i+\frac{1}{2},j}}{\Delta\tau} - \mathcal{L}^{\eta}_{i+\frac{1}{2},j}(U,\Delta V) = \mathcal{L}^{\eta}_{i+\frac{1}{2},j}(U,V) - \mathcal{D}^{\eta}_{i+\frac{1}{2},j}(\omega). \tag{25}$$

In equations (24) and (25) $\mathcal{V}_U$ and $\mathcal{V}_V$ are the velocity-component control volumes (EFGH and ILMN in Figure 2, respectively), $\Delta\tau$ is the pseudo-time step and ΔU, ΔV are the unknowns, namely, the variations of the dependent variables from the old to the new iteration level; $\mathcal{L}^{\xi}$, $\mathcal{D}^{\xi}$, $\mathcal{L}^{\eta}$ and $\mathcal{D}^{\eta}$ are shorthand notations for the diffusion-like operators and the vorticity coupling terms for the U and V equations, respectively. The discretization of the operators in equations (24) and (25) is performed according to Pascazio and Napolitano (1996), so as to produce steady-state solutions satisfying conditions (2) and (3) exactly in the discrete. They are given as:

$$\begin{aligned}\mathcal{L}^{\xi}_{i,j+\frac{1}{2}}(U,V) = \boldsymbol{S}^{\xi}\cdot\Big[&(\nabla\times\boldsymbol{u}\times\boldsymbol{S}^{\eta})_{j+1} - (\nabla\times\boldsymbol{u}\times\boldsymbol{S}^{\eta})_{j}\\ &+ (\nabla\cdot\boldsymbol{u}\boldsymbol{S}^{\xi})_{i+\frac{1}{2}} - (\nabla\cdot\boldsymbol{u}\boldsymbol{S}^{\xi})_{i-\frac{1}{2}}\Big],\end{aligned} \tag{26}$$

$$\mathcal{D}^{\xi}_{i,j+\frac{1}{2}}(\omega) = \boldsymbol{S}^{\xi}\cdot\Big[(\omega\boldsymbol{k}\times\boldsymbol{S}^{\eta})_{j+1} - (\omega\boldsymbol{k}\times\boldsymbol{S}^{\eta})_{j}\Big], \tag{27}$$

$$\begin{aligned}\mathcal{L}^{\eta}_{i+\frac{1}{2},j}(U,V) = \boldsymbol{S}^{\eta}\cdot\Big[&(\nabla\times\boldsymbol{u}\times\boldsymbol{S}^{\xi})_{i+1} - (\nabla\times\boldsymbol{u}\times\boldsymbol{S}^{\xi})_{i}\\ &+ (\nabla\cdot\boldsymbol{u}\boldsymbol{S}^{\eta})_{j+\frac{1}{2}} - (\nabla\cdot\boldsymbol{u}\boldsymbol{S}^{\eta})_{j-\frac{1}{2}}\Big],\end{aligned} \tag{28}$$

$$\mathcal{D}^{\eta}_{i+\frac{1}{2},j}(\omega) = \boldsymbol{S}^{\eta}\cdot\Big[(\omega\boldsymbol{k}\times\boldsymbol{S}^{\xi})_{i+1} - (\omega\boldsymbol{k}\times\boldsymbol{S}^{\xi})_{i}\Big]. \tag{29}$$

Equations (24)-(25) are solved by an alternating direction line-Gauss-Seidel relaxation procedure combined with a coarse-grid-correction multigrid scheme Brandt (1982) using full weighting collection and bilinear prolongation operators (see Napolitano and Pascazio (1991)). It is noteworthy that, using the inner iteration procedure to couple the vorticity and velocity fields, the discrete continuity and vorticity-definition equations are satisfied within $\mathcal{O}(\epsilon)$.

2.3 Results

The well-known Taylor problem (Batchelor, 1960), having the analytical solution:

$$\begin{aligned} u &= -\cos x\,\sin y\, e^{-2t/Re},\\ v &= \sin x\,\cos y\, e^{-2t/Re},\\ \omega &= 2\cos x\,\cos y\, e^{-2t/Re},\end{aligned} \tag{30}$$

has been used at first to verify the accuracy of the proposed numerical scheme. The problem has been solved in a square domain $[0,\pi/2]^2$, for $0 \le t \le 1$ and

$Re = 10$. Numerical results have been obtained on uniform grids with $(N + 1) \times (N + 1)$ points and N_t time steps, for several values of N and N_t, maintaining N/N_t constant. The numerical errors at the final time, $t = 1$, have been computed as the L^1 norms of the differences between the computed and exact solutions. The corresponding orders of accuracy are then evaluated according to

$$p = \frac{\ln(\text{error}_H/\text{error}_h)}{\ln(H/h)}.$$

Tables I and II provide the values of the errors and of the corresponding orders of accuracy for four values of N and N_t, without and with the inner iteration procedure ($\epsilon = 10^{-6}$), respectively. It is clear that the inner iteration procedure increases the order of the time accuracy from 1 to 2, as expected, while tripling the CPU time.

The impulsively started symmetric flow past a circular cylinder has been considered, for two different values of the Reynolds number (based on the cylinder diameter), namely, $Re = 40$ and $Re = 550$. A stretched cylindrical grid is employed ($r = r_{\text{out}} + (r_{\text{out}} - r_{\text{cil}}) \tanh [2 (\eta - \eta_{\max})/(\eta_{\max} - 1)]/ \tanh 2$), the outer boundary being at a distance of 40 diameters away from the cylinder, with 129×129 grid-points and $\Delta t = 0.05$. Figure 3 shows the separation length obtained for $Re = 40$ together with the numerical results of Collins and

	ω		U		V	
N, N_t	error	p	error	p	error	p
8,10	0.1304 (–1)		0.3394 (–2)		0.3470 (–2)	
		0.7334		1.150		1.041
16, 20	0.7843 (–2)		0.1530 (–2)		0.1686 (–2)	
		0.8997		1.046		1.146
32, 40	0.4204 (–2)		0.7410 (–3)		0.7619 (–3)	
		0.9365		1.028		1.050
64, 80	0.2196 (–2)		0.3634 (–3)		0.3679 (–3)	

Table I. Taylor's problem. Solution obtained *without* the inner iteration procedure

	ω		U		V	
N, N_t	error	p	error	p	error	p
8, 10	0.5891 (–2)		0.5909 (–3)		0.5294 (–3)	
		1.940		2.042		1.992
16, 20	0.1535 (–2)		0.1435 (–3)		0.1331 (–3)	
		2.015		2.042		2.027
32, 40	0.3800 (–3)		0.3484 (–4)		0.3266 (–4)	
		2.050		2.040		2.048
64, 80	0.9169 (–4)		0.8472 (–5)		0.7893 (–5)	

Table II. Taylor's problem. Solution obtained *with* the inner iteration procedure

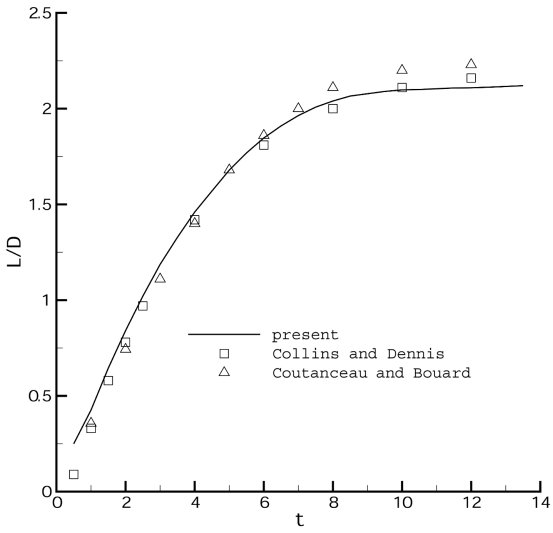

Figure 3.
Flow past a circular cylinder for $Re = 40$: separation length versus t

Dennis (1973). The experimental data of Coutanceau and Bouard (1977) are also given for completeness. The time evolution of the separation length for $Re = 550$ is shown in Figure 4 together with the numerical results of Loc (1980) and the experimental data of Bouard and Coutanceau (1980). In both cases, the present solutions are in good agreement with both the aforementioned numerical and experimental results.

It is noteworthy that the same results of Figures 3 and 4, within plotting accuracy, have been obtained without the inner iteration procedure, using the same grids and $\Delta t = 0.005$. Thus, the second-order scheme roughly provides a threefold efficiency improvement with respect to the first-order one.

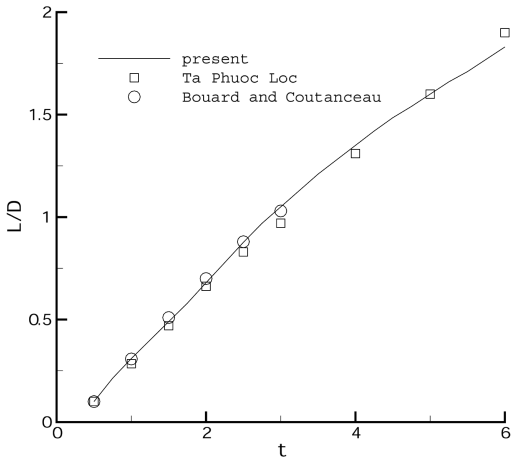

Figure 4.
Flow past a circular cylinder for $Re = 550$: separation length versus t

2.4 Conclusion

An accurate and efficient technique for solving the unsteady two-dimensional vorticity-velocity Navier-Stokes equations in general curvilinear coordinates has been presented. The governing equations, written as a system of a scalar transport equation for the vorticity and two second-order elliptic equations for the velocity components, are discretized in space by a staggered-grid second-order-accurate finite-volume method. The vorticity equation is discretized in time using a three-level scheme and the resulting discrete system is factorized by an alternating direction implicit method. At each time step, the velocity field is then computed by a very efficient multigrid line-Gauss-Seidel relaxation scheme. An inner iteration loop to evaluate the wall vorticity at the new time level allows one to achieve second-order accuracy in time. The theoretical accuracy of the method is first verified towards a test case having an analytical solution. Then, solutions to unsteady flows past a circular cylinder are presented, which are in good agreement with both experimental and numerical results available in the scientific literature. The proposed scheme is now being extended to three space dimensions.

3. Compressible flows

3.1 Governing equations

The unsteady two-dimensional Reynolds-averaged Navier-Stokes equations, closed by the $k-\omega$ turbulence-model (Wilcox, 1988, 1994), are given by:

$$\frac{\partial U}{\partial t} + \frac{\partial (F_i^c - F_i^v)}{\partial x_i} = S, \tag{31}$$

where U is the vector of the conservative variables,

$$U = \begin{pmatrix} \rho \\ \rho u_i \\ \rho E \\ \rho k \\ \rho \omega \end{pmatrix}, \tag{32}$$

F_i^c are the components of the convective fluxes,

$$F_i^c = \begin{pmatrix} \rho u_i \\ p\delta_{ij} + \rho u_i u_j \\ \rho u_i H \\ \rho u_i k \\ \rho u_i \omega \end{pmatrix}, \tag{33}$$

and F_i^v are the components of the viscous fluxes,

$$F_i^v = \begin{pmatrix} 0 \\ \hat{\tau}_{ij} \\ b_i \\ (\mu + \sigma^\star \mu_t) \dfrac{\partial k}{\partial x_i} \\ (\mu + \sigma \mu_t) \dfrac{\partial \omega}{\partial x_i} \end{pmatrix}. \tag{34}$$

In equation (31), S is the vector of the source terms, given as:

$$S = \begin{pmatrix} 0 \\ 0 \\ 0 \\ \tau_{ij} \dfrac{\partial u_i}{\partial x_j} - \beta^\star \rho \omega k \\ \frac{\alpha\omega}{k} \tau_{ij} \dfrac{\partial u_i}{\partial x_j} - \beta \rho \omega^2 \end{pmatrix}. \tag{35}$$

In equations (31-35), u_i are the components of the velocity vector and p, ρ, k and ω are the pressure, density, turbulence kinetic energy and turbulence specific dissipation rate, respectively; E and H are the specific total internal energy and the specific total enthalpy, $E = e + k + u_i u_i/2$, $H = h + k + u_i u_i/2$; μ is the dynamic viscosity coefficient and μ_t is the eddy viscosity coefficient. In equation (34), $\hat{\tau}$ is the tensor of the viscous and Reynolds stresses,

$$\hat{\tau}_{ij} = 2\mu \left[\frac{1}{2} \left(\frac{\partial u_i}{\partial x_j} + \frac{\partial u_j}{\partial x_i} \right) - \frac{1}{3} \frac{\partial u_k}{\partial x_k} \delta_{ij} \right] + \tau_{ij}, \tag{36}$$

where τ_{ij} is the Reynolds stress tensor given as:

$$\tau_{ij} = 2\mu_t \left[\frac{1}{2} \left(\frac{\partial u_i}{\partial x_j} + \frac{\partial u_j}{\partial x_i} \right) - \frac{1}{3} \frac{\partial u_k}{\partial x_k} \delta_{ij} \right] - \frac{2}{3} \rho k \delta_{ij}. \tag{37}$$

Furthermore, the energy fluxes in equation (34) are given as:

$$b_i = u_j \tau_{ij} + \left(\frac{\mu}{Pr} + \frac{\mu_t}{Pr_t} \right) \frac{\partial h}{\partial x_i} + (\mu + \sigma^\star \mu_t) \frac{\partial k}{\partial x_i}, \tag{38}$$

where Pr and Pr_t are the laminar and turbulent Prandtl numbers, respectively. Concerning the two viscosity coefficients, μ is evaluated using Sutherland's law, whereas

$$\mu_t = \frac{\alpha^\star \rho k}{\omega}. \tag{39}$$

The six closure parameters $\alpha^\star, \alpha, \beta^\star, \beta, \sigma^\star$ and σ are computed according to the low-Reynolds number $k-\omega$ turbulence-model (Wilcox, 1994):

$$\alpha^\star = \frac{\alpha_0^\star + Re_t/R_k}{1 + Re_t/R_k}, \tag{40}$$

$$\alpha = \frac{5}{9}\ \frac{\alpha_0 + Re_t/R_\omega}{1 + Re_t/R_\omega}\ \alpha^{\star -1}, \tag{41}$$

$$\beta^\star = \frac{9}{100}\ \frac{5/18 + (Re_t/R_\beta)^4}{1 + (Re_t/R_\beta)^4}, \tag{42}$$

$$\beta = 3/40, \qquad \sigma^\star = \sigma = 1/2, \tag{43}$$

$$\alpha_0^\star = \beta/3, \qquad \alpha_0 = 1/10, \tag{44}$$

$$R_\beta = 8, \qquad R_k = 6, \qquad R_\omega = 2.7, \tag{45}$$

where Re_t is the turbulent Reynolds number, defined as:

$$Re_t = \frac{\rho k}{\omega \mu}. \tag{46}$$

Finally, an equation of state is required to complete the governing equations. In the present work, the equation of state for perfect gases has been employed,

$$p = (\gamma - 1)\left[\rho E - \rho \frac{u_i u_i}{2} - \rho k\right], \tag{47}$$

where γ is the specific heat ratio.

3.2 Boundary conditions

Standard characteristic boundary conditions are imposed at inflow and outflow boundaries. For the case of subsonic flow, which is considered in the present work, the total enthalpy, total pressure, flow angle, turbulence kinetic energy and turbulence specific dissipation rate are imposed at inlet points, whereas pressure is prescribed at outlet points. In particular, the value of k at inlet points is evaluated as follows:

$$k_{in} = \frac{3}{2}(u_{in} Tu_{in})^2, \tag{48}$$

whereas the value of the turbulence specific dissipation rate at inlet points corresponds to a turbulence length scale about equal to $10^{-2}g$, where g is the cascade pitch. Furthermore, at solid wall, no slip wall boundary condition is

used and the turbulence kinetic energy is set to zero. The pressure and the temperature at the wall are computed by forcing zero normal gradients. Concerning the value of ω at the wall, the following condition has been employed (see Menter and Rumsey (1994):

$$\omega_w = 10\frac{6\nu}{\beta(\Delta y_w)^2}, \tag{49}$$

where ν is the kinematic viscosity coefficient and Δy_w is the distance between the wall and the first grid-point away from the wall. As pointed out by Wilcox (1988), the $k-\omega$ model gives the correct smooth wall behavior if $\omega_w > 100u_\tau^2/\nu$, where $u_\tau = \sqrt{\tau_w/\rho_w}$ is the friction velocity. The condition (49) satisfies such a requirement, provided that $y_w^+ < 3$. For cascade flow computations, boundary conditions are also needed to impose flow periodicity at the mid-channel boundary and at the branch-cut, when using C-grids. In particular, in the present work, non-periodic C-grids are employed, namely the two edges of the branch-cut have not the same number of cells. This feature allows one to obtain a low distortion of the mesh in the blade channel. A conservative treatment of the boundary conditions at the branch-cut is applied by using two rows of phantom cells, overlapping the grid, in which the dependent variables are evaluated by linear interpolation, from regular-cell values.

3.3 Space discretization

The computational domain is subdivided into non-overlapping quadrilateral cells. Integrating equation (31) over each cell Ω_j and using Green's theorem, one has:

$$\frac{\partial}{\partial t}\int_{\Omega_j} U\, d\Omega + \oint_{\partial\Omega} \mathbf{F}\cdot \boldsymbol{n} d\ell = \int_{\Omega_j} S\, d\Omega, \tag{50}$$

where $\boldsymbol{n}$ is the outward unit normal to the boundary $\partial\Omega$ of Ω_j and $\boldsymbol{F} = (F_1^c - F_1^v, F_2^c - F_2^v)$. The semi-discrete form of equation (50) reads:

$$\frac{d}{dt}U_j = \frac{-1}{\Omega_j}\sum_{k=1}^{4}(\boldsymbol{F}\cdot\boldsymbol{n})_{j,k}\ell_{j,k} + S_j = -R_j(U), \tag{51}$$

where the summation is extended to the four edges of the quadrilateral cell Ω_j and $\ell_{j,k}$ represents the length of the kth edge. A strongly coupled approach is employed for solving equation (51); namely, the Navier-Stokes equations and the turbulence-model equations are solved as a unique set. The convective fluxes at each interface are evaluated using a flux difference splitting method:

$$(\boldsymbol{F}\cdot\boldsymbol{n})_{j,k} = F_n = \frac{1}{2}\left[(F_n)_R + (F_n)_L - \sum \mid \Delta F_n \mid\right], \tag{52}$$

where $(F_n)_R$ and $(F_n)_L$ are evaluated using the right and left states with respect to the interface. The flux differences, $|\Delta F_n|$, in equation (52) are evaluated as follows:

$$
\begin{aligned}
|\Delta F_n| = |\hat{\overline{u}}|(\Delta\rho - \frac{\Delta p}{\hat{a}^2}) & \begin{bmatrix} 1 \\ \hat{u}_i \\ \frac{\hat{u}_i\hat{u}_i}{2} + \hat{k} \\ \hat{k} \\ \hat{\omega} \end{bmatrix} \\
+ |\hat{\overline{u}}| \hat{\rho} & \begin{bmatrix} 0 \\ \Delta u_i - n_i\Delta\overline{u} \\ \hat{u}_i\Delta u_i - \overline{u}\Delta\overline{u} + \Delta k \\ \Delta k \\ \Delta\omega \end{bmatrix} \\
+ |\hat{\overline{u}} \pm \hat{a}| \frac{\Delta p \pm \hat{\rho}\hat{a}\Delta\overline{u}}{2\hat{a}^2} & \begin{bmatrix} 1 \\ \hat{u}_i \pm n_i\hat{a} \\ \hat{H} \pm \hat{\overline{u}}\hat{a} \\ \hat{k} \\ \hat{\omega} \end{bmatrix},
\end{aligned}
\tag{53}
$$

where a is the speed of sound, $\overline{u} = \mathbf{u} \cdot \mathbf{n}$, $\hat{(\cdot)}$ indicates Roe-averaged variables (Roe, 1981; Morrison and Gatski, 1993) and $\Delta(\cdot) = (\cdot)_R - (\cdot)_L$. Initial data for the Riemann problem at each interface are computed using a formally second-order-accurate upwind MUSCL extrapolation with minmod limiter. The diffusive contributions in equation (51) are evaluated employing central differencing: at each interface the derivatives of the primitive variables are computed using Green's theorem and a dual cell centered at the interface; whereas the required flow variables are obtained averaging adjacent cell-center values. Finally the derivatives employed to evaluate the source terms, S_j, are obtained using Green's theorem over the cell Ω_j.

3.4 Time discretization

In order to exploit the techniques developed to improve the efficiency of explicit methods for steady-state problems (such as local time stepping, residual smoothing and multigrid strategy), while retaining the time accuracy, equation (51) are reformulated following the methodology proposed in Jameson (1983):

$$
\frac{d}{dt^\star} U_j + R_j^\star(U) = 0, \tag{54}
$$

with

$$R_j^{\star}(U) = \frac{3U_j^{n+1} - 4U_j^n + U_j^{n-1}}{2\Delta t} + R_j(U^{n+1}), \tag{55}$$

where $t^{\star}$ indicates a fictitious time, whereas the index n refers to the physical time t. The steady-state solution of equation (54), with respect to the fictitious time, is equivalent to the implicit solution of equation (51), where the time derivative has been discretized using a three-level backward formula which is second-order-accurate in time. At each physical time step the solution is advanced in the fictitious time, by means of an explicit four-stage Runge-Kutta scheme with coefficients: $\alpha_1 = 1/4$, $\alpha_2 = 1/3$, $\alpha_3 = 1/2$, accelerated by local time stepping, implicit residual smoothing and multigrid. The time step used for all equation (54) is evaluated as:

$$\Delta t^{\star} = CFL \frac{\Delta t^{\star c} \Delta t^{\star v}}{\Delta t^{\star c} + \Delta t^{\star v}}, \tag{56}$$

where CFL indicates the Courant-Friedrichs-Lewy number and the convective, $\Delta t^{\star c}$, and diffusive, $\Delta t^{\star v}$, fictitious time steps are computed according to Arnone *et al.* (1995). At each stage of the Runge-Kutta scheme the residuals are smoothed according to the variable-coefficient implicit procedure proposed in (Martinelli and Jameson (1988); Cicatelli and Sieverding (1997), which allows a value of *CFL* equal to 4 in the present calculations. Moreover, convergence of equation (54) to any desired accuracy level is accelerated by a V-cycle FAS multigrid strategy using bilinear interpolation and full weighting collection. It is noteworthy that, in the turbulence transport equations, the eddy viscosity is updated only at the end of each Runge-Kutta step and is kept frozen at the intermediate stages; the critical production and dissipation terms are computed only on the finest grid-level and transferred to the coarser ones.

3.5 Results

The subsonic turbulent flow through a large-scale nozzle guide vane has been considered as a test problem. The blade has a front-loaded-type design, with a moderate turning and a straight rear suction side, which ensures a turbulent state of the suction side boundary layer at the trailing edge. Each blade has a thick rounded trailing edge, which causes the formation of a von Karman vortex street due to the unsteady separation of the boundary layers. Cicatelli and Sieverding (1997), Manna *et al.* (1997) and Sieverding and Heinemann (1990) provided high quality unsteady experimental data which are suitable for the validation of numerical methods for the solution of the Navier-Stokes equations. The main geometrical features of the cascade are: chord length, c = 280mm; pitch to chord ratio, g/c = 0.696; trailing edge thickness to chord ratio, D/c = 0.0536; stagger angle, $\gamma = -49°83$. The blade coordinates are provided in Manna *et al.* (1997). The overall blade dimensions for the experimental test are determined by the need for a high spatial resolution at the

trailing edge. Owing to the relatively small aspect ratio, two fences were placed close to the end-wall boundary layers in order to prevent the formation of secondary flows. In this way two-dimensional flow conditions exist over approximately 75 per cent of the blade height. Furthermore a 0.4mm trip-wire was located on the pressure side at x/c_{ax} = 0.61 in order to guarantee a turbulent boundary layer at the trailing edge. The flow conditions are: inlet total temperature, T_{01} = 293K; inlet total pressure, p_{01} = 1.178bar; isentropic exit Mach number, $M_{2,is}$ = 0.4; turbulence intensity, Tu = 1.15 per cent. Reynolds number, $Re = 2.8\times10^6$. The Reynolds number is based on the axial chord and on outlet-flow conditions. Concerning the reference experimental data reported in Manna *et al.* (1997); Sieverding and Heinemann (1990), wall pressure tappings were employed to determine the velocity distribution along the blade profile, whereas a rotatable cylinder, equipped with a fast response pressure transducer, was inserted in the trailing edge at the blade midspan to measure pressure oscillations. Figure 5 shows the reference system for the data representation used in Manna *et al.* (1997); Sieverding and Heinemann (1990), the center of the trailing edge being the origin of such a system. The data are reported with respect to either the angular position or the curvilinear abscissa non-dimensionalized by the trailing edge diameter, s/D. Unsteady computations were performed using three C-meshes with 256×32, 384×48 and 576×72 quadrilateral cells, having 128, 192 and 288 cells along the profile, respectively; the corresponding average y^+ values at the first cell center close to the blade profile are 2.3, 1 and 0.5. The coarse grid is shown in Figure 6. Three and four multigrid levels were employed for the coarse and the other grids, respectively. Between two consecutive physical instants, the L^1 norm of the residual of the continuity equation was reduced to 10^{-5}, requiring from ten to 25 multigrid V-cycles, depending on the grid employed. The computation of one physical time step, using the finest grid, required about 300 seconds on a Digital Ultimate (single processor) computer. Computations were performed using three different time steps, corresponding to about 30, 60 and 90 divisions of the shedding period, respectively, without noticing any remarkable difference in the amplitude and period of the pressure fluctuations. A global view of the flow is provided in Figures 7 and 8, where the instantaneous Mach number and density (non-dimensionalized with respect to the inlet total density ρ_{01}) contours, computed using the fine grid, are shown. In Figures 9 and 10 the

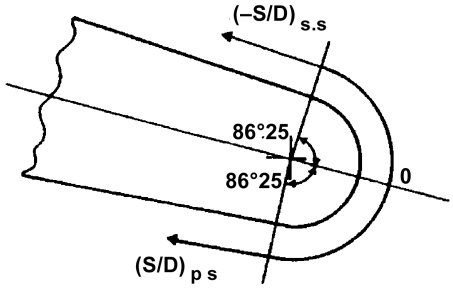

Figure 5.
Reference system at the trailing edge

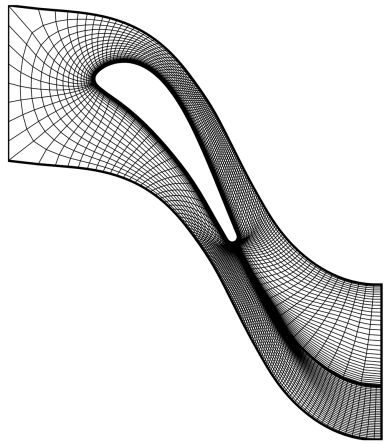

Figure 6.
Computational grid (256 × 32)

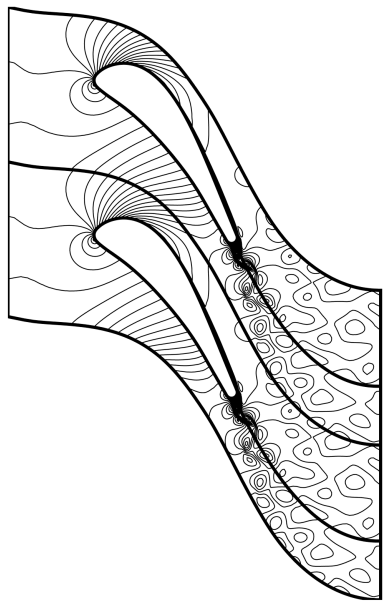

Figure 7.
Mach number contours on the finest grid ($\Delta M = 0.02$)

computed pressure time-histories at two different locations are provided. The curves refer to the finest grid computations, a similar behavior being obtained using the other grids. After an initial time interval, a well defined cyclic behavior is reached. The pressure fluctuations induced by the vortex shedding propagates far upstream in the boundary layers, as has also been found by experiments (Manna *et al.,* 1997; Sieverding and Heinemann, 1990). Furthermore, the computations confirm that the largest pressure oscillation is obtained on the pressure side of the blade. Nevertheless, a discrepancy exists between experimental and computed data concerning the amplitude of the pressure oscillations. Concerning the experimental unsteady flow data

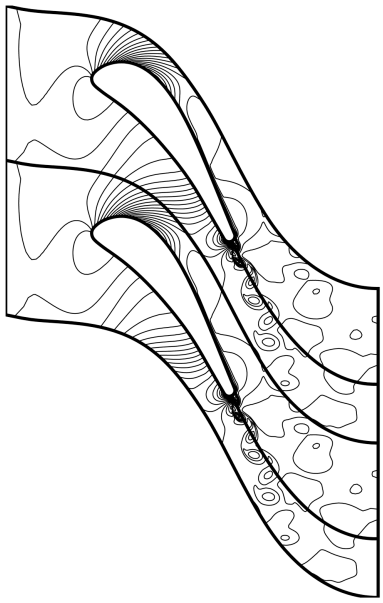

Figure 8.
Density contours on the finest grid ($\Delta(\rho/\rho_0) = 0.005$)

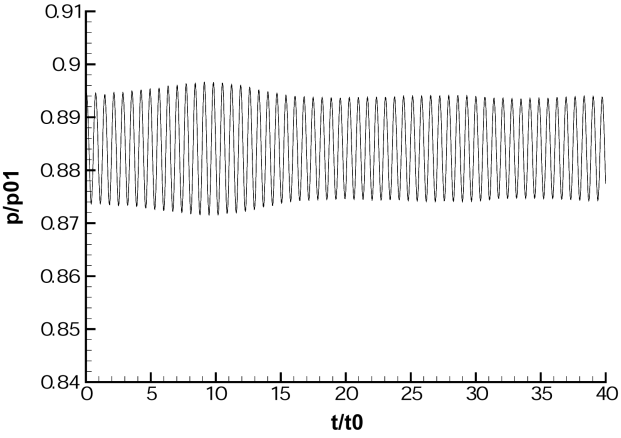

Figure 9.
Pressure time-history at $s/D = -1.7$

provided in Manna *et al.* (1997); Sieverding and Heinemann (1990), the pressure signal at $s/D = 0.48$ has been recorded. The associated dominant frequency is 2.65kHz, which corresponds to a Strouhal number (based on the trailing edge diameter and on the isentropic exit velocity) equal to 0.297. The computed dominant frequencies are 1.87kHz, 2.13kHz, 2.31kHz, for the coarse, medium and fine grid, respectively, which correspond to Strouhal numbers equal to 0.208, 0.237 and 0.256. Employing the Richardson extrapolation based on the medium and fine grid values, a Strouhal number equal to 0.274 is obtained. The numerical values are slightly lower than the experimental data, but all fall in the typical range of blades with fully turbulent boundary layers on both sides

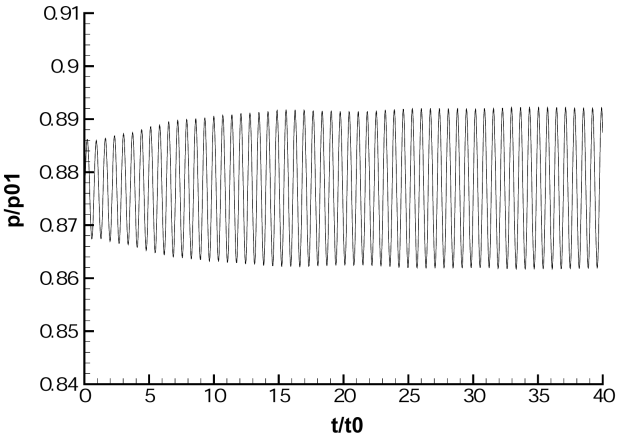

Figure 10.
Pressure time-history at $s/D = 1.67$

of the trailing edge. The isentropic Mach number distributions along the blade profile are shown in Figure 11. The symbols refer to the experimental data of Manna *et al.* (1997), whereas the lines refer to the computed results. In particular, the time averaged (over 40 cycles) distributions obtained using the coarse, medium and fine grid are represented. The numerical results agree quite well with the experimental data, the lines corresponding to the medium and fine grid being coincident within plotting accuracy. The curve corresponding to the coarse grid is very close to the previous ones except in the region of the trailing edge where an unphysical sudden over-compression is predicted due to the low grid resolution. The time averaged pressure distribution at the trailing is shown in Figure 12. The pressure is non-dimensionalized with respect to the inlet total pressure p_{01} and it is drawn

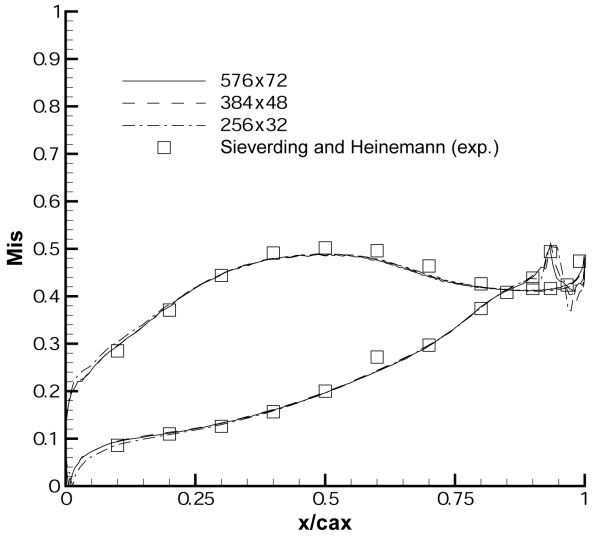

Figure 11.
Isentropic Mach number distribution

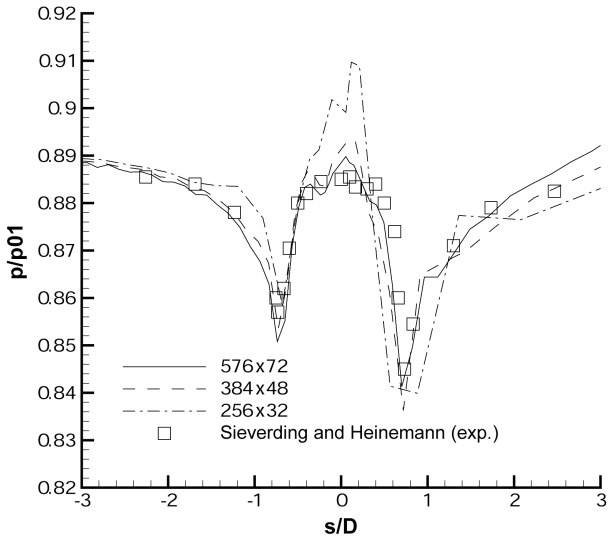

Figure 12.
Pressure distribution at the trailing edge

versus the curvilinear abscissa of Figure 5. The computed results show a clear trend toward grid convergence, and the line corresponding to the fine grid agrees quite well with the experimental data. It is noteworthy that the maximum difference between the experimental data and the fine-grid solution is about 1 per cent of the inlet total pressure. The space averaged value of the base pressure between $s/D = \pm 0.4$ is equal to 0.8847 versus the experimental value equal to 0.885.

It is noteworthy that, with respect to the present test problem, this method is certainly less efficient than that of Arnone *et al.* (1995), using central differences and artificial dissipation. However, for problems involving moving shocks, the additional cost of Roe's FDS space discretization is worth paying. Moreover, a third-order accurate MUSCL differencing can be introduced in the present approach with minimum additional computational work.

4. Conclusion

A strongly coupled approach for solving the unsteady Reynolds-averaged Navier-Stokes equations with $k - \omega$ turbulence closure has been presented. A finite-volume space discretization is used, the convective terms being approximated by means of Roe's scheme, with three-point upwind MUSCL extrapolation, and the diffusive ones by standard central differences. Second-order accuracy in time is achieved using a dual time stepping technique, in which the false-transient residual at every time level is evaluated by an explicit Runge-Kutta scheme with multigrid acceleration. The method has been validated versus the unsteady flow through a turbine cascade. The method is being extended to three space dimensions to analyze secondary flows through turbomachinery cascades.

References and further reading

Arnone, A., Liou, M. and Povinelli, L.A. (1995), "Integration of Navier-Stokes equations using dual time stepping and a multigrid method", *AIAA J.*, Vol. 33 No. 6, pp. 985-90.

Batchelor, G.K. (Ed.) (1960), *The Collected Works of G.I. Taylor*, Cambridge University Press, Cambridge.

Beam, R.M. and Warming, R.F. (1978), "An implicit factored scheme for the compressible Navier-Stokes equations", *AIAA J.*, Vol. 16, pp. 393-402.

Beam, R.M. and Warming, R.F. (1980), "Alternating direction implicit methods for parabolic equations with a mixed derivative", *SIAM J. Sci. Stat. Comput.*, Vol. 1, pp. 131-59.

Bouard, R. and Coutanceau, M. (1980), "The early stage of development of the wake behind an impulsively started cylinder for $40 < Re < 10^4$", *J. Fluid Mech.*, Vol. 101, pp. 583-607.

Brandt, A. (1982), "Guide to multigrid development", *Lecture Notes in Mathematics*, 960, Springer Verlag, Berlin, pp. 220-312.

Cicatelli, G. and Sieverding, C.H. (1997), "The effect of vortex shedding on the unsteady pressure distribution around the trailing edge of a turbine blade", *ASME Journal of Turbomachinery*, Vol. 119, pp. 810-19.

Collins, W.M. and Dennis, S.C.R. (1973), "Flow past an impulsively started circular cylinder", *J. Fluid Mech.*, Vol. 60, p. 105.

Coutanceau, M. and Bouard, R. (1977), "Experimental determination of the main features of the viscous flow in the wake of a circular cylinder in uniform translation. Part 2. Unsteady flow", *J. Fluid Mech.*, Vol. 79, pp. 257-72.

Fasel, H. (1976), "Investigation of the stability of boundary layers by a finite-difference model of the Navier-Stokes equations", *J. Fluid Mech.*, Vol. 78, pp. 355-83.

Gatski, T.B., Grosch C.E. and Rose M.E. (1989), "The numerical solution of the Navier-Stokes equations for 3-dimensional, unsteady, incompressible flows by compact schemes", *J. Comput. Phys.*, Vol. 82, pp. 298-329.

Jameson, A. (1983), "Transonic flow calculations", *MAE Report, 1651*, Mechanical and Aerospace Engineering Department, Princeton University, Princeton, NJ.

Jameson, A. (1991), "Time dependent calculations using multigrid, with applications to unsteady flows past airfoils and wings", *AIAA Paper, 91-1596*.

Loc, Ta Phuoc (1980), "Numerical analysis of unsteady secondary vortices generated by an impulsively started circular cylinder", *J. Fluid Mech.*, Vol. 100, pp. 101-28.

Manna, M., Mulas, M. and Cicatelli, G. (1997), "Vortex shedding behind a blunt trailing edge blade", *International Journal of Turbo and Jet Engines*, Vol. 14, pp. 145-57.

Martinelli, L. and Jameson, A. (1988), "Validation of a multigrid method for the Reynolds averaged equations", *AIAA Paper, 88-0414*.

Menter, F.R. and Rumsey, C.L. (1994), "Assessment of two-equation turbulence models for transonic flows", *AIAA Paper, 94-2343*.

Morrison, J. and Gatski, T. (1993), "Solution of compressible, turbulent transport equations using a flux-difference split scheme", *Lecture Notes in Physics*, 414, Springer Verlag, Berlin/Heidelberg, pp. 180-84.

Napolitano, M. and Pascazio, G.A. (1991), "A numerical method for the vorticity-velocity Navier-Stokes equations in two and three dimensions", *Comput. Fluids*, Vol. 19, pp. 489-95.

Osswald, G.A., Ghia, K.N. and Ghia, U.A (1987), "A direct algorithm for solution of incompressible three-dimensional unsteady Navier-Stokes equations", *Proc. AIAA 8th Computational Fluid Dynamics Conference*, AIAA, Washington, DC, pp. 408-21.

Pascazio, G. and Napolitano, M. (1996), "A staggered-grid finite volume method for the vorticity-velocity equations", *Comput. Fluids*, Vol. 25, pp. 433-46.

Roe, P.L. (1981), "Approximate Riemann solvers, parameter vectors and difference schemes", *J. Comput. Phys.*, Vol. 43 No. 2, October.

Sieverding, C.H. and Heinemann, H. (1990), "The influence of boundary layer state on vortex shedding from flat plates and turbine cascades", *ASME Journal of Turbomachinery*, Vol. 112, pp. 181-7.

Wilcox, D.C. (1988), "Reassessment of the scale-determining equation for advanced turbulence models", *AIAA J.*, Vol. 26 No. 11, pp. 1299-310.

Wilcox, D.C. (1994), "Simulation of transition with a two equation turbulence model", *AIAA J.*, Vol. 32 No. 2, pp. 247-55.